Supporting Information

Hydration-driven Structural Reorganization and Switchable Thermal-Photoinduced Spin-State Dynamics in Iron(II) Spin-crossover Crystalline Solids

Mousumi Dutta[1], Ajana Dutta[2], Pradip Chakraborty[1,3]*

[1]Department of Chemistry, Indian Institute of Technology Kharagpur, Kharagpur-721302, India

[2]Department of Physics, Indian Institute of Technology Kharagpur, Kharagpur-721302, India

[3]School of Nano Science and Technology, Indian Institute of Technology Kharagpur, Kharagpur-721302, India

*Corresponding Author, E-mail: pradipc@chem.iitkgp.ac.in

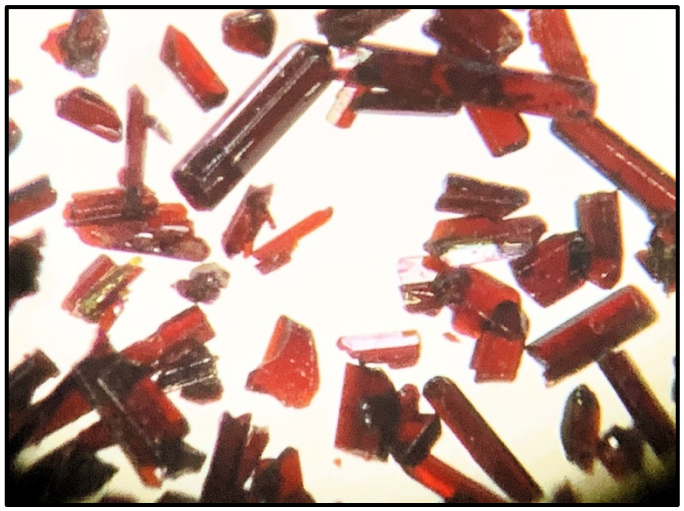

Figure S1: Picture of the as-synthesized reddish-brown rod-shaped crystals (under microscope) of $[Fe(3\text{-bpp})_2]_2[Cr(ox)_3](ClO_4)\cdot 5H_2O$ (Compound **1**) grown *via* liquid-to-liquid diffusion.

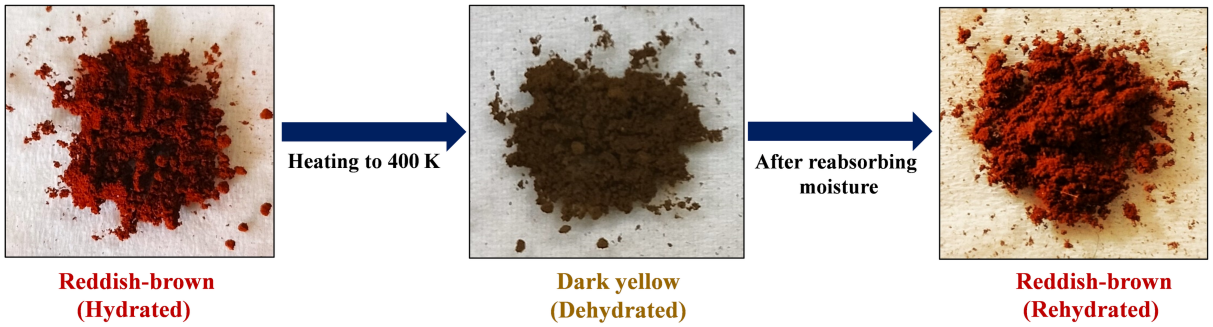

Figure S2: Crystals derived powders exhibit reversible color changes, changing from reddish-brown (left) at room temperature (hydrated) to dark yellow (middle) upon heating to 400 K (dehydrated). The original color was restored when the sample reabsorbs moisture (rehydrated) under ambient conditions (right).

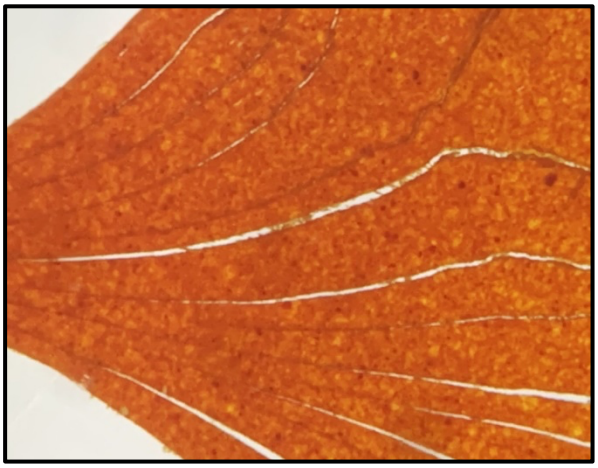

Figure S3: The image shows a small section of a thin, optically transparent pellet (under microscope) obtained by crushing the single crystal into a fine powder, thoroughly mixing it with IR-grade KBr, and then pressing under hydraulic press.

Table S1: Relevant crystallographic parameters for Compound **1** at 100 K (**1a**) and at 296 K (**1b**).

	1a	**1b**
CCDC No.	2452703	2452704
Chemical formula	C50 H46 Cl Cr Fe2 N20 O21	C50 H46 Cl Cr Fe2 N20 O21
Formula Weight	1462.22	1462.22
T [K]	100(2)	296(2)
Radiation, λ [Å]	0.71073	0.71073
Color	Reddish-brown	Reddish-brown
Crystal system	Orthorhombic	Orthorhombic
Space group	$Pca2_1$	$Pca2_1$
Z	4	4
a (Å)	22.4221(5)	22.526(3)
b (Å)	16.1769(4)	16.3717(18)
c (Å)	16.3909(4)	16.5570(18)
V (Å^3)	5945.3(2)	6106.0(12)
ρ_{calcd} (mg/m^3)	1.634	1.591
μ (mm^{-1})	0.802	0.781
F(000)	2988	2988
Crystal size (mm^3)	0.100 × 0.080 × 0.060	0.100 × 0.080 × 0.060
2θ range (◦) for data collection	1.552 to 27.623°	1.538 to 25.806°
Completeness	100.0 %	100.0 %
Index range, h, k, l	-29 ≤ h ≤ 29, -21 ≤ k ≤ 21, -21 ≤ l ≤ 21	-27 ≤ h ≤ 27, -19 ≤ k ≤ 19, -20 ≤ l ≤ 20
Reflections collected	145743	145190
Independent reflections	13796	11697
Data / restraints / parameters	13796 / 173 / 900	11697 / 389 / 943
Goodness-of-fit on F^2	1.029	1.042
R_{int}	0.0552	0.0852
R_1, wR_2 [I > 2σ(I)]	0.0298, 0.0723	0.0488, 0.1132
R_1, wR_2 [all data]	0.0338, 0.0744	0.0611, 0.1201
Largest diff. peak/hole [eÅ^{-3}]	1.468 and -0.760	1.271 and -1.137

Table S2: A list of selective bond lengths for Compound **1** at 100 K (**1a**) and at 296 K (**1b**).

	1a	**1b**
Temp. [K]	100(2)	296(2)
V [Å^3]	5945.3(2)	6106.0(12)
Bond lengths [Å]		
$Fe^{II}1$-N2	1.952(3)	1.959(5)
$Fe^{II}1$-N3	1.957(3)	1.957(5)
$Fe^{II}1$-N5	1.910(3)	1.915(5)
$Fe^{II}1$-N6	1.912(3)	1.903(5)
$Fe^{II}1$-N8	1.955(3)	1.969(5)
$Fe^{II}1$-N9	1.955(3)	1.957(5)
$Fe^{II}1$-N (Average)	1.940(3)	1.943(5)
$Fe^{II}2$-N12	1.964(3)	1.987(6)
$Fe^{II}2$-N13	1.964(3)	1.966(6)
$Fe^{II}2$-N15	1.920(3)	1.919(5)
$Fe^{II}2$-N16	1.926(3)	1.943(6)
$Fe^{II}2$-N18	1.974(3)	1.992(5)
$Fe^{II}2$-N19	1.949(3)	1.964(5)
$Fe^{II}2$-N (Average)	1.950(3)	1.962(5)
Cr-O (Average)	1.977(2)	1.979(6)
Trans-N5– $Fe^{II}1$–N6 angle (φ)	179.8(13)	179.9(3)
Trans-N15– $Fe^{II}2$–N16 angle (φ)	176.1(11)	175.9(2)
Dihedral angle (θ)-N2-$Fe^{II}1$-N9	91.5(11)	91.7(2)
Dihedral angle (θ)-N18-$Fe^{II}2$-N13	93.2(11)	93.1(2)

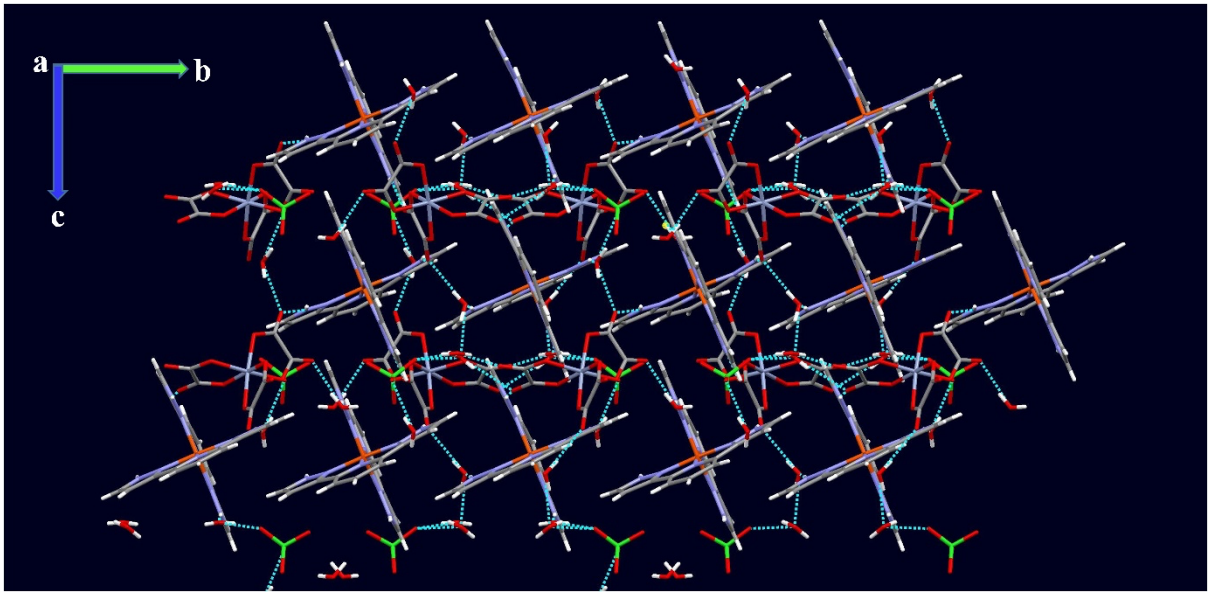

Figure S4a: Well-defined layered crystal packing pattern for compound **1** at 100 K upon growing the unit cell, showing 3-bpp ligands engaging in H-bonding through their non-coordinating -NH groups with the $[Cr(ox)_3]^{3-}$ and ClO_4^- anions, and five water molecules. Alternating cationic and anionic layers are shown in the structure.

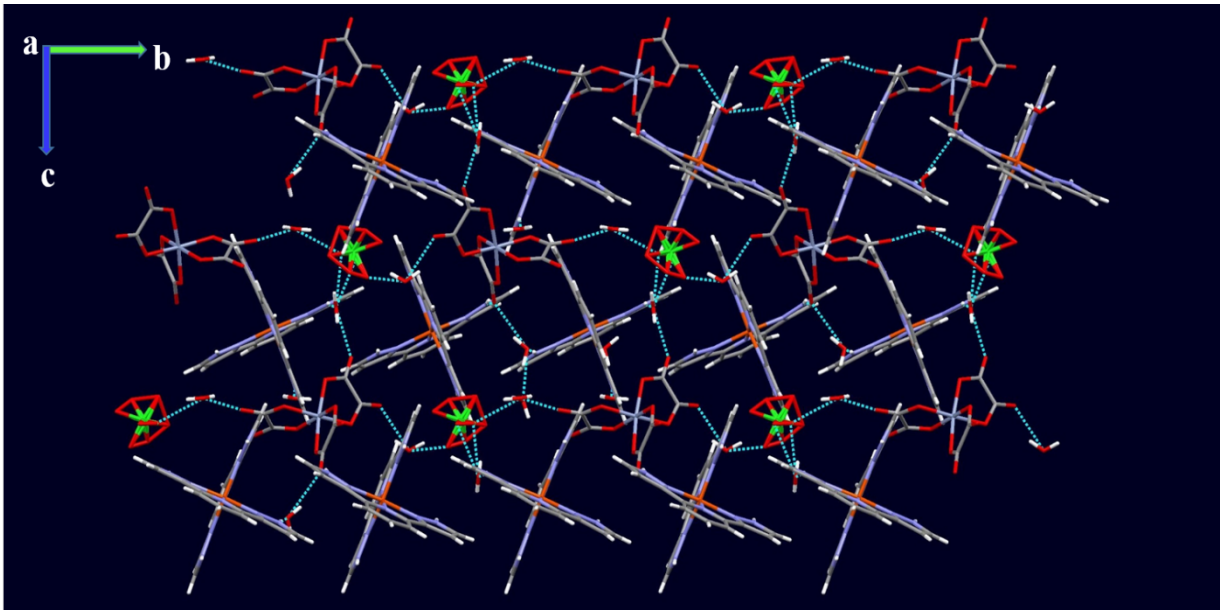

Figure S4b: Well-defined layered crystal packing pattern for compound **1** at 296 K upon growing the unit cell, showing 3-bpp ligands engaging in H-bonding through their non-coordinating -NH groups with the $[Cr(ox)_3]^{3-}$ and ClO_4^- anions, and five water molecules. Alternating cationic and anionic layers are shown in the structure. Notably, the ClO_4^- anion is disordered at room temperature.

Powder X-ray diffraction (PXRD)

The experimental room-temperature PXRD pattern (red, Figure S5a) closely matches the simulated pattern generated from single-crystal XRD data (black), with peak indexing performed using *X'Pert High Score Plus* (v4.8). Major diffraction peaks are labeled in Figure S5a. Le Bail profile fitting, carried out in *JANA2006* based on the orthorhombic room-temperature single-crystal structure, further confirm structural consistency and phase purity (Figure S5b). Table S3 lists the refined unit cell parameters at different temperatures. Starting values (a = 22.526(3) Å, b = 16.3717(1) Å, c = 16.5570(1) Å, $Pca2_1$, Z = 4) refine to a = 22.5858(2) Å, b = 16.3757(2) Å, c = 16.5671(1) Å with χ^2 = 1.04, R_p = 2.85, and R_{wp} = 3.98. The sharp Bragg reflections confirm high crystallinity, and the excellent agreement between observed (Y_{obs}) and calculated (Y_{cal}) profiles establishes the bulk phase purity of Compound **1**, which is subsequently used for further studies.

Table S3. Cell parameters of the refined PXRD data with refinement indicators at different experimental temperatures for Compound **1**.

Temperature [K]	**296**	**350 (Heating)**	**400 (Heating)**	**350 (Cooling)**
Crystal system	Orthorhombic	Orthorhombic	Tetragonal	Orthorhombic
Space group	$Pca2_1$	$Pca2_1$	P_4	$Pca2_1$
Refined cell parameters	a = 22.5858(2) Å b = 16.3757(2) Å c = 16.5671(1) Å	a = 22.6218(1) Å b = 16.5633(2) Å c = 16.7450(1) Å	$a = b$ = 16.7195(3) Å c = 26.7329(5) Å	a = 22.3865(2) Å b = 16.5666(2) Å c = 16.7799(1) Å
Volume (Å^3)	6127.5(1)	6274.2(1)	7472.94(8)	6223.1(5)
R_p	2.85	3.21	2.03	1.96
R_{wp}	3.98	6.02	3.69	3.53
χ^2	1.04	3.21	1.89	1.90

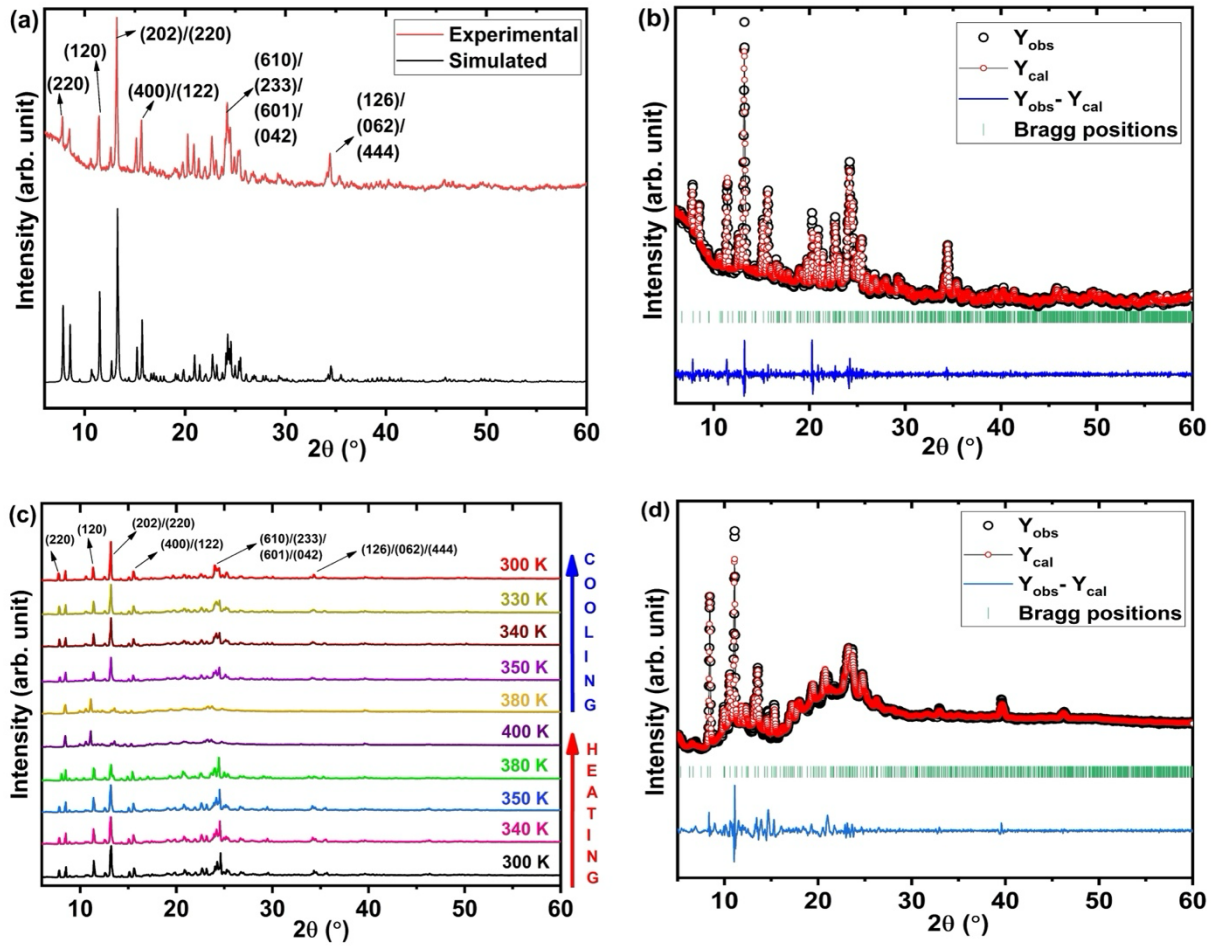

Figure S5. (a) Room temperature experimental PXRD patterns of Compound **1** with major peaks indexed shown at the top panel (red) along with the simulated pattern at the bottom (black) obtained from single-crystal data for comparison, **(b)** PXRD Le bail profile refinement at room temperature, **(c)** Variable temperature PXRD pattern between 300 and 400 K, and **(d)** Le bail profile refinement of high-temperature PXRD at 400 K (Compound **1**.WF).

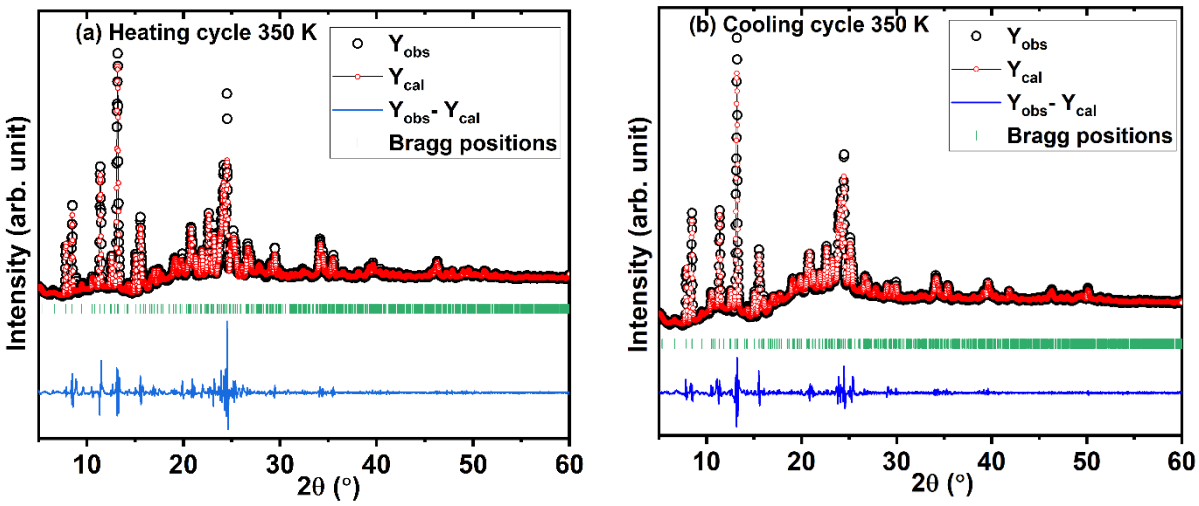

Figure S6: (a) Profile refinement of the high temperature PXRD of $[Fe(3\text{-}bpp)_2]_2[Cr(ox)_3](ClO_4)\cdot 5H_2O$ at 350 K in the heating cycle. Refined cell parameters are a = 22.6218(1) Å, b = 16.5633(2) Å and c = 16.7450(1) Å in $Pca2_1$ space group. **(b)** Profile refinement of the high temperature PXRD of $[Fe(3\text{-}bpp)_2]_2[Cr(ox)_3](ClO_4)\cdot 5H_2O$ at 350 K in the cooling cycle. Refined cell parameters are a = 22.3865(2) Å, b = 16.5666(2) Å and c = 16.7799(1) Å in $Pca2_1$ space group.

Thermogravimetric Analysis (TGA)

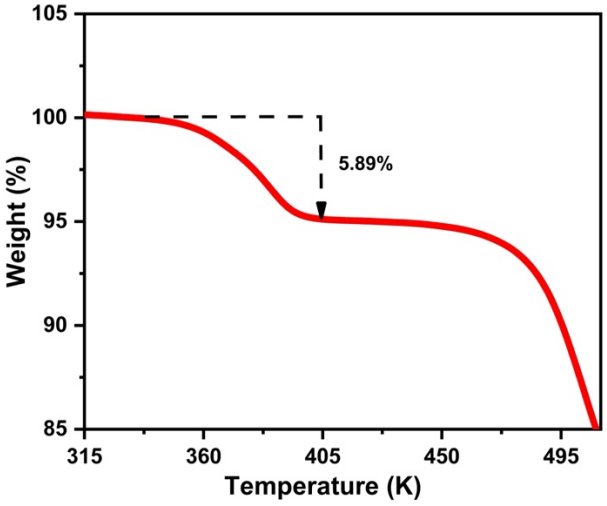

Figure S7: Thermogravimetric analysis (TGA) plot of Compound **1**

Thermogravimetric analysis (TGA) of Compound **1**, conducted under a dry nitrogen atmosphere, shows a distinct weight loss attributable to dehydration (Figure S7). The measured weight loss of 5.89% closely matches the content of five water molecules identified through single-crystal

X-ray diffraction analysis. This dehydration begins at approximately 375 K, indicating that the water molecules are uncoordinated and easily removed upon heating. These results provide valuable insight into the thermal behavior and structural characteristics of Compound **1**, underscoring its sensitivity to temperature and the reversible nature of its hydration state.

Fourier Transform Infrared (FTIR) spectroscopy

To further verify the presence of water in Compound **1**, FTIR analysis is performed, as shown in Figure S8. A broad O−H stretching band around 3400 cm^{-1} confirms the hydrated nature of the compound. Moreover, the appearance of the following specific IR bands uniquely confirms the formation of the target compound in its hydrated phase, Fe-N ($\nu_{Str.}$) ~ 536 cm^{-1} (s); Cr-O ($\nu_{Str.}$) ~ 766 cm^{-1} (s); Cl-O ($\nu_{Str.}$) ~ 618 cm^{-1} (m) and 1091 cm^{-1} (s); -OH ($\nu_{Str.}$) ~ 3552, 3422 cm^{-1}.

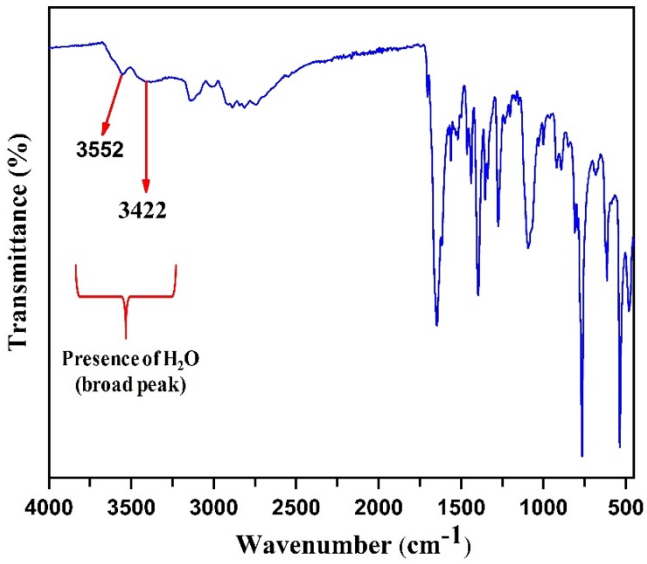

Figure S8: FTIR spectra of the as-synthesized compound **1**.

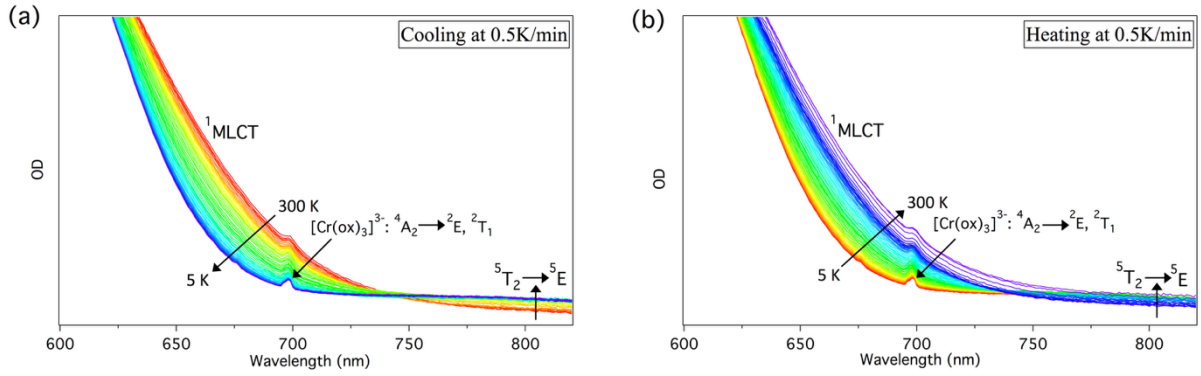

Figure S9. Temperature-dependent single-crystal optical absorption spectra of hydrated $[Fe(3\text{-bpp})_2]_2[Cr(ox)_3](ClO_4)\cdot 5H_2O$, recorded at a sweep rate of 0.5 K/min. **(a)** Spectral evolution during cooling from 300 K to 5 K (solid rainbow-colored lines). **(b)** Spectral evolution during the subsequent heating cycle back to 300 K (solid rainbow-colored lines). The evolution of the low-lying ^{1}MLCT absorption band is monitored throughout both the thermal spin transition process. A sharp but weak absorption peak at 697 nm is attributed to the $^4A_2 \rightarrow {}^2E, {}^2T_1$ spin-flip transition of Cr(III) in the $[Cr(ox)_3]^{3-}$ moiety. A weak band around 800 nm corresponds to the characteristic $^5T_2 \rightarrow {}^5E$ transition of the Fe(II) high-spin (HS) state.

Figures S9a and S9b show high-resolution absorption spectra of a hydrated single crystal of compound **1** (dimensions ~ 0.25 × 0.15 × 0.1 mm^3) recorded during controlled cooling (300 → 5 K) and heating (5 → 300 K) at 0.5 K/min. Spectra are collected with incident light perpendicular to the crystal surface, monitoring the evolution of MLCT bands in the 625–700 nm region. Two distinct MLCT transitions are observed: the LS-associated $^1A_1 \rightarrow {}^1$MLCT band (635–680 nm, extending beyond 700 nm) and the HS-associated $^5T_2 \rightarrow {}^5$MLCT band (625–660 nm, tailing near 700 nm). Below 620 nm (LS) and 600 nm (HS), the spectra become saturated. A weak, sharp feature at 697 nm, assigned to the spin-forbidden $^4A_2 \rightarrow {}^2E, {}^2T_1$ transition of $[Cr(ox)_3]^{3-}$, remains temperature-invariant. Absorbance near 625 nm, corresponding to the high-energy edge of the LS-MLCT band, serves as a marker for spin-state changes.

During cooling, the intensity of the HS ^{5}MLCT band unexpectedly increases and shifts to higher energy, indicating a growing HS population, corroborated by the appearance of a weak

HS ^{5}dd band near 800 nm (marked by arrows in Figure S9a and S9b). On heating, the system fully reverts to the LS state, confirming reversibility.

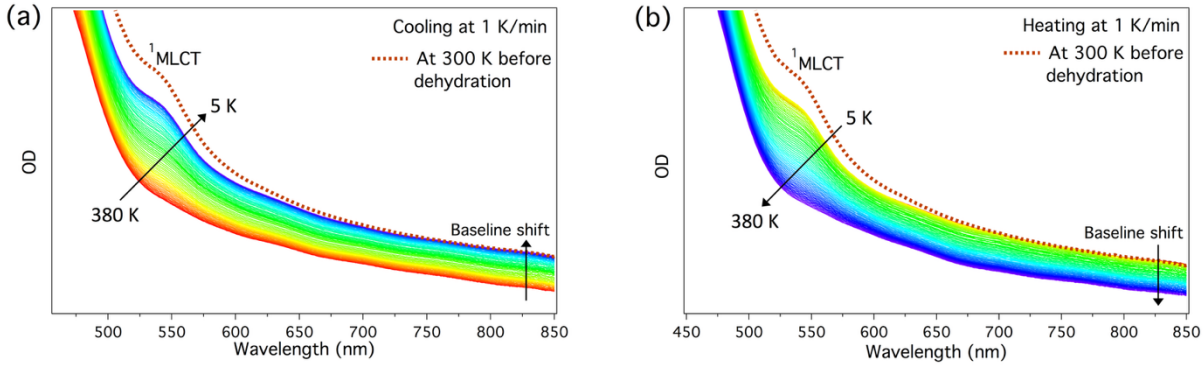

Figure S10. Temperature-dependent high-resolution absorption spectra of a powder sample of dehydrated $[Fe(3\text{-bpp})_2]_2[Cr(ox)_3](ClO_4)$, dispersed in an optically transparent thin KBr pellet, recorded at a scan rate of 1 K/min during **(a)** cooling and **(b)** heating cycles between 380 K and 5 K. The evolution of the low-lying ^{1}MLCT absorption band is tracked throughout the thermal spin switching. The brown dotted spectrum represents the absorption profile at 300 K before dehydration and serves as the reference for the pure low-spin (LS) state. Baseline shifts are indicated by upward arrows during cooling and downward arrows during heating.

Photoinduced HS → LS relaxation behavior: hydrated vs dehydrated phase

To probe the relaxation dynamics of the photoinduced HS state, time-resolved spectral evolution is recorded during HS → LS relaxation in the hydrated phase at 4, 7, 10, 13, 16, and 20 K (Figures S11a–f). The HS state is generated by irradiating the sample at 4 K with a 632 nm cw laser (~ 2 mW/mm^2, 5 min), converting the kinetically trapped mixed state ($\gamma_{HS} \approx 0.25$) to a fully populated HS state via LIESST (pink spectrum in each panel). For relaxation measurements, the sample is rapidly heated to the target temperature (except at 4 K), and the decay is monitored spectroscopically. After each run, the sample is recooled to 4 K and the irradiation–relaxation cycle repeated to ensure reproducibility. The evolution of the ^{1}MLCT shoulder band near 625 nm is used to track the HS → LS relaxation. The spectra show that relaxation kinetics remain of the same order of magnitude across all measured temperatures: at

higher T the HS → LS decay occurs within accessible timescales, while at lower T it slows modestly but remains detectable within the experimental window. In addition to spectral intensity changes, a consistent baseline shift is observed during relaxation at all temperatures. This effect is attributed to enhanced diffuse scattering caused by random domain or cluster formation linked to structural reorganization, crystallographic phase transitions, or major crystal packing changes involving the two Fe(II) SCO centers. These results are consistent with baseline effects noted in previous T(LIESST) studies.[55, 72]

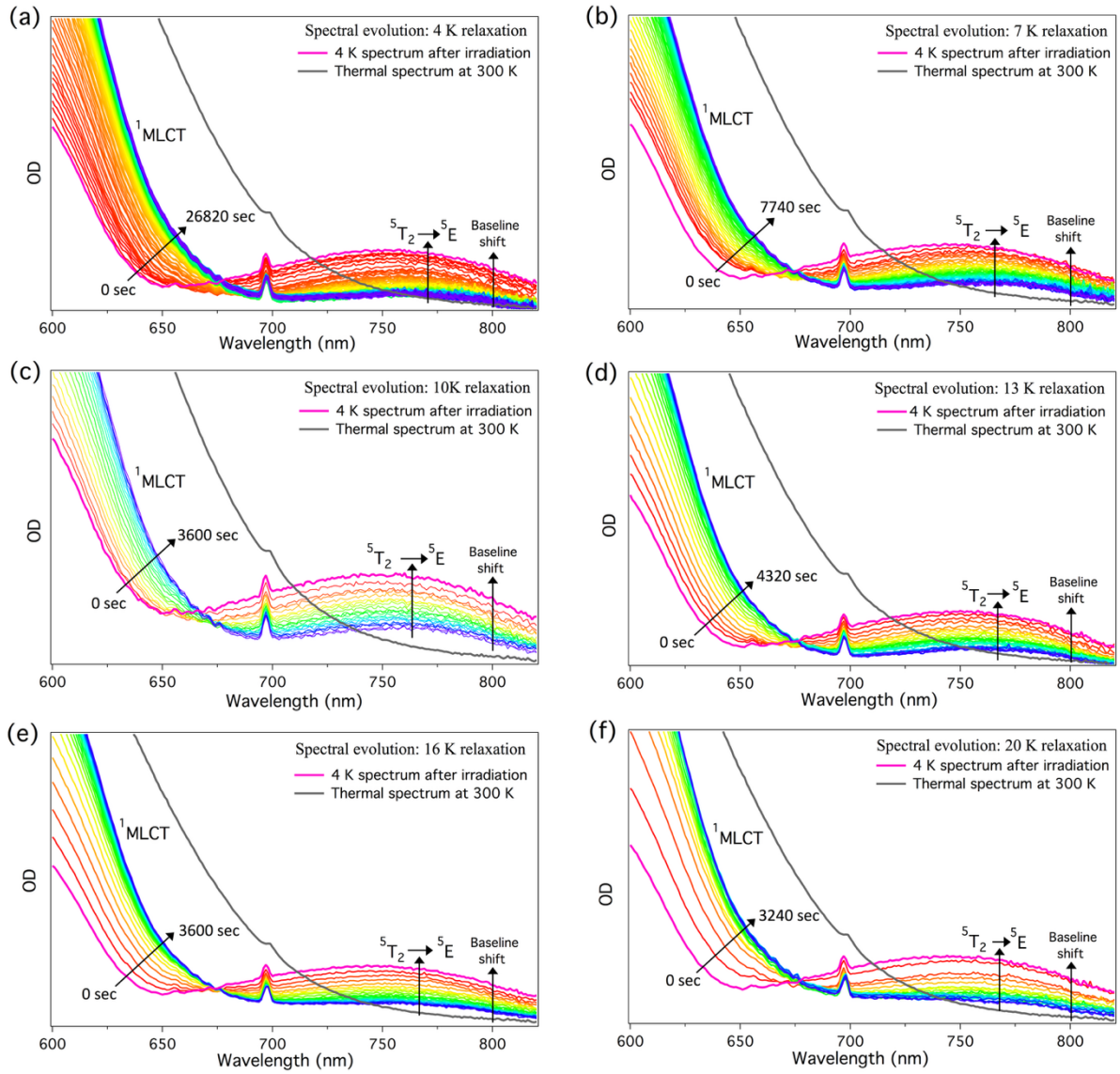

Figure S11. Time-resolved single-crystal absorption spectra of hydrated $[Fe(3\text{-bpp})_2]_2[Cr(ox)_3](ClO_4)\cdot 5H_2O$, measured during light-induced high-spin (HS) to low-spin (LS)

relaxation at selected temperatures (4, 7, 10, 13, 16, and 20 K), following LIESST excitation at 4 K with 632 nm laser (2 mW/mm^2). The progression of spectral changes reflects the gradual relaxation from the light-induced HS state to the LS state at a target experimental temperature. A black vertical arrow highlights the baseline shift associated with this relaxation process. The gray spectrum represents the thermally populated LS state at 300 K and serves as a reference for the pure LS state. A weak band around 800 nm corresponds to the characteristic $^5T_2 \rightarrow {}^5E$ transition of the Fe(II) high-spin (HS) state.

To probe the dehydrated phase, HS → LS relaxation is studied alongside the T(LIESST) experiment. Figure S12 presents time-resolved spectra monitored at 55 K, 60 K, 65 K and 70 K. The HS state is generated by 532 nm cw laser irradiation at 4 K (5 mW/mm^2, 5 min), converting the partially stabilized state ($\gamma_{HS} \approx 0.30$) into the fully populated HS state via LIESST (pink spectrum). For reference, the pure LS spectrum recorded at 300 K before dehydration is shown as the brown dotted line.

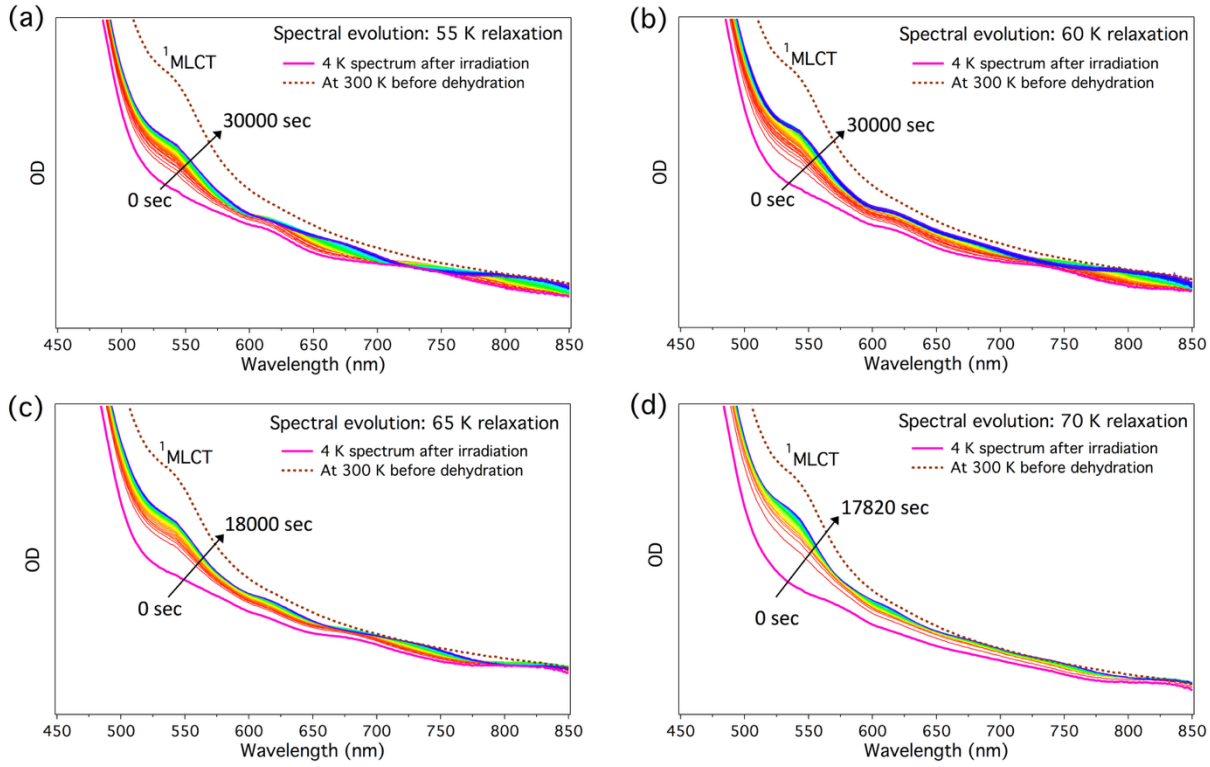

Figure S12. Time-resolved high-resolution absorption spectra of a powder sample of dehydrated [Fe(3-bpp)$_2$]$_2$[Cr(ox)$_3$](ClO$_4$), dispersed in a transparent KBr pellet, recorded during light-induced high-spin (HS) to low-spin (LS) relaxation at selected temperatures (55, 60, 65, and 70 K). The spectra are

collected following LIESST excitation at 4 K using a 532 nm laser (nominal power 5 mW/mm^2). At each temperature, the spectral evolution reflects the gradual relaxation from the photoinduced HS state back to the LS state. The black arrow indicates the direction of time progression, starting from t = 0 s and extending to t = 30,000 s (55 and 60 K), 18,000 s (65 K), and 17,820 s (70 K). The brown dotted spectrum corresponds to the thermally populated LS state at 300 K and serves as a reference for the pure LS state.

As in the hydrated phase, the dehydrated sample is rapidly warmed to the target relaxation temperature immediately after photoexcitation. After each measurement, the crystal is recooled to 4 K and the irradiation-relaxation cycle repeated to ensure reproducibility. The HS → LS relaxation is monitored by tracking the ^{1}MLCT shoulder band near 538 nm. As shown in Figure S12, the relaxation kinetics display minimal temperature dependence across the studied range. A consistent feature at all temperatures is the appearance of interference patterns, also observed during the T(LIESST) process. These arise from enhanced diffuse scattering caused by random domain or cluster formation associated with structural reorganization, crystallographic phase transitions, or major rearrangements in crystal packing involving the two Fe(II) SCO centers.[72, 76]